Honorable Mention Poster Award

Ultrasound Self-Calibration

Emad M. Boctor, Iulian Iordachita, Gabor Fichtinger and Gregory D. Hager

Computer-Integrated Surgical Systems and Technologies (CISST)
Engineering Research Center, Johns Hopkins University
eboctor@ieee.org, {iordachita., gabor@cs., hager@cs.}jhu.edu

ABSTRACT

This paper describes a new robust method for 2D and 3D ultrasound (US) probe calibration using a closed-form solution. Prior to calibration, a position sensor is attached to the probe and is used to tag each image/volume with its position and orientation in space. At the same time, image information used to determine target location in probe coordinates. The calibration procedure uses these two pieces of information to determine the transformation (translation, rotation, and scaling) of the scan plane with respect to the position sensor. We introduce a novel methodology for real-time in-vivo quality control of tracked US systems, in order to capture registration failures during the clinical procedure. In effect, we dynamically recalibrate the tracked US system for rotation, scale factor, and in-plane position offset up to a scale factor. We detect any unexpected change in these parameters through capturing discrepancies in the resulting calibration matrix, thereby assuring quality (accuracy and consistency) of the tracked system. No phantom is used for the recalibration. We perform the task of quality control in the background, transparently to the clinical user while the subject is being scanned. We present the concept, mathematical formulation, and experimental evaluation in-vitro. This new method can play an important role in guaranteeing accurate, consistent, and reliable performance of tracked ultrasound.

Keywords: 3DUS, Ultrasound Calibration, Image Guided Surgery, Robotic Ultrasound, Quality control.

1. INTRODUCTION

During the past two decades surgical procedures have witnessed a revolutionary change, nowadays referred to as Computer Integrated Surgery. In particular, with the introduction of various imaging modalities such as Magnetic Resonance Imaging (MRI), Computer Tomography (CT), and Ultrasound (US), surgical procedures have seen advancement in all stages, pre-, post-, and –intra-operative alike. True 3D imaging modalities, like MRI and CT, are extremely potent in terms of their rendering capabilities, but are cumbersome to use for intra-operative procedures, mainly due to obstructive hardware and imaging latency. Ultrasound, however, has been emerging as a widely popular image guidance modality, since it is real-time, safe, convenient to use in the operating room, and readily inexpensive compared to CT and MRI.

Unfortunately, conventional ultrasound is predominantly a 2D imaging methodology. A significant amount of research has been conducted to convert this technology to provide the physicians with a 3D real-time visualization of the internal anatomy [1]. There are two basic methods to achieve this. The first, an intrinsically 3D method, is to either employ a fixed two-dimensional array transducer or a uniformly moving single array of sensors. This approach is somewhat limited, because the scanning range is constrained by the hardware, which is quite often rather bulky and expensive. The second technique, an indirectly 3D method, is to let the clinician manually acquire spatially co-registered 2D image slices, compound those into a contiguous 3D volume [2], and then refresh the volume with real-time slices. This approach is highly applicable to tracking invasive surgical tools and compensating for organ motion. Significant research has been dedicated to quantitative tracked ultrasound, involving tracking the US probe in 3D space with respect to a stationary frame of reference. While tracked US originates from interventional applications, it recently has become an indispensable tool in external beam radiation therapy (EBRT) guidance [3]. In fact, EBRT is expected to become the largest user of tracked ultrasound in the next couple of years. Each year in the United States 65,000 patients

Medical Imaging 2006: Visualization, Image-Guided Procedures, and Display,
edited by Kevin R. Cleary, Robert L. Galloway, Jr., Proc. of SPIE Vol. 6141, 61412N, (2006)
1605-7422/06/$15 · doi: 10.1117/12.659594

are treated for prostate cancer alone. Considering an average of 40 treatment fractions per patient, the total number of procedures is approximately 2.6 million a year. Tracked US guidance is also applicable to the EBRT of breast cancer, adding about 2 million more cases to the potential market.

Typically, tracking is achieved by rigidly attaching 3D localizers to the US probe. A missing link, however, is the spatial transformation between the US image pixels and the 3D localizers on the probe, which requires calibration. Hence, calibration is ubiquitously present in all systems where ultrasound is used for quantitative image guidance. From our experience, the wide majority of intra-operative hazard situations in tracked US systems are caused by failure of registration between tracking and imaging coordinate frames, thereby manifesting in miscalibration of the tracked US. The most typical form of error is a false reading of the tracker. This occurs quite often in electromagnetic tracking systems due to invisible field distortions caused by metal objects or electromagnetic noise. Another typical problem related to tracking is deformation or physical damage of the tracking body attached to the probe, causing a latent misreading of pose. What makes these problems exceedingly dangerous is that they occur without apparent warning. Among human operator errors, inadvertent changes of lateral image polarity occur quite frequently and transparently to the clinical user. With regular off-line recalibration some of the aforementioned errors can be caught prior to procedure. The process is called Quality Control (QC), a mandatory routine in any clinical department. Typically, QC is performed annually, monthly, or weekly, which places a heavy financial burden on the department. In addition to increasing patient safety, reduction in QC costs clearly is a major incentive.

In all current calibration methods, a set of objects (often referred to as phantoms) with known geometrical properties are scanned and then various mathematical procedures are applied to estimate the unknown transformation that maximizes the similarity between the US images and the phantom [4-9, 13]. There is error associated with each stage of the process (phantom fabrication, image acquisition, spatial co-registration, image processing, formulation, and numerical optimization solution), the combined total error of which may easily become significant. Geometrical model based phantoms like points [4-6, 10, 11] and planes [5, 7, 11] exist and some studies have compared their accuracy and performance [5, 11]. The cross-wire and three-wire phantoms require large numbers of images and are hard to automate, while the single-wall phantom such as the Cambridge phantom [5] is a more automatic, repeatable method. Figure 1 shows a typical formulation for the coordinate systems required for the fore mentioned phantoms. Galloway *et al.* [9] introduced pointer-based methods, which simplify the nonlinear optimization problem. However, these methods require pointer calibration and careful data collection. One variation of the pointer-based method was introduced by Pagoulatos [6], where the phantom is a collection of N-shaped fiducials that are defined in the tracker frame. Blackall *et al.* [12] presented a voxel based registration method for US calibration. Registration is achieved by the maximization of normalized mutual information. This occurs when accurate calibration parameters give optimal similarity between the US images of the phantom and the 3D voxel based model acquired pre-operatively.

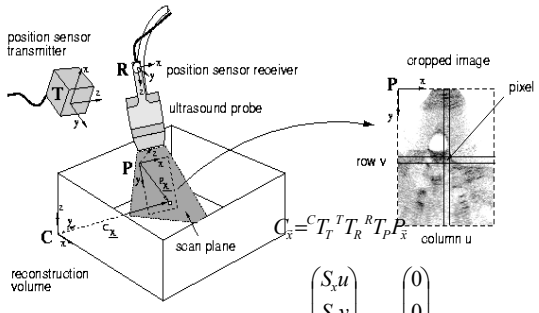

Figure 1: The chain of transformations is from pixel frame P, to the receiver frame R, to transmitter frame T, and finally to construction frame C. The (u,v) pixel coordinates are multiplied by (Sx,Sy) scale factors. The resulting transformed point Cx has the (0,0,0) coordinate values [Cross-wire Phantom]. (Upper figure Courtesy of R. Prager)

The use of special objects and phantoms, however, is cumbersome and foreign to the operating room where interrupting the procedure for the sake of probe calibration is not practical. What is required therefore is a paradigm shift in calibration technology to a phantomless self-calibration that is performed directly on the patient, intra-operatively, in real-time, transparently to the physician.

Generally, full calibration involves a six degree-of-freedom (DOF) rigid transformation and three or two dimensional scale factors when using 3DUS or 2DUS probes, respectively. However, on a practical level, the possibility of pure translational error in the calibration matrix is low. One atypical scenario would involve the rigidly attached sensor sliding without experiencing any relative rotation in the US image reference frame. Thus for the purpose of QC, it is sufficient to recalibrate the system for the remaining (rotational and scale) degrees-of-freedom. This paper presents the concept, mathematical framework, experimental implementation, and in-vitro evaluation of a phantomless real-time method that detects intra-operative failures of the tracked US while recovering the calibration matrix.

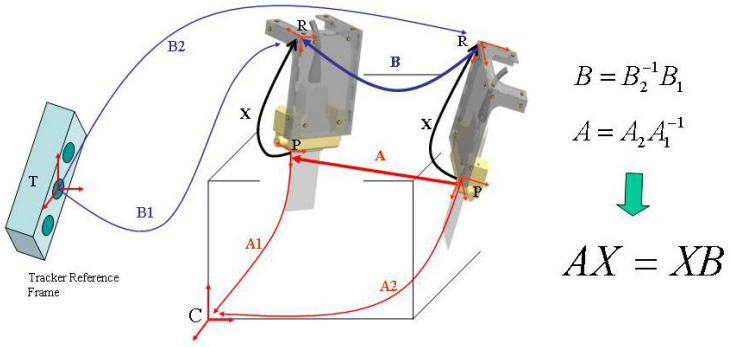

Figure 2: Coordinate definitions in the closed form $AX=XB$.

2. MATHEMATICAL FORMULATION

The key enabler of our self-calibration method is a closed-form mathematical formulation of the problem. Figure 2 presents the coordinate systems for the mathematical formulation. A_1, A_2 are the transformations of US picture coordinate system (P) with respect to the fixed construction frame (C) at poses 1 and 2, respectively. Note that the actual selection of C is arbitrary and the only requirement is that it must be rigidly fixed during the calibration process. Using A_1 and A_2, we obtain the transformation between poses 1 and 2, as $A=A_2A_1^{-1}$. At the same time, the transformation between the two poses can be recovered using a calibration phantom or recovered directly by matching the 2D ultrasound images acquired in these poses to a prior 3D model of the phantom object. B_1 and B_2 are readings from the tracker for the sensor frame (R) with respect to tracker reference frame (T), at poses 1 and 2 respectively. The relative pose between the sensor frame (R) at pose 1 and 2 is given by $B = B_2^{-1}B_1$. This yields the following homogeneous matrix equation:

$$AX = XB, \text{which is:} \quad \textbf{1}.\text{a}$$

$$R_a R_x = R_x R_b, \text{and} \quad \textbf{2}.\text{b}$$

$$R_a t_x + D(u_a)\vec{\lambda} = R_x t_b + t_x \quad \textbf{3}.\text{c}$$

Where A is estimated from images, B is assumed to be known from the external tracking device, and X is the unknown transformation between the US image coordinate system and the sensor frame (R). Expanding this equation yields two separate constraints on translation and rotation, where R_a is the rotation of the US image frame between pose 1 and 2, λ is the unknown scale factor vector that relates the translation vector u_a in voxel space to the US image frame translation vector t_a (usually expressed in mm), such that:

$$t_a = \begin{pmatrix} \lambda_x u_{ax} \\ \lambda_y u_{ay} \\ \lambda_z u_{az} \end{pmatrix} = \begin{pmatrix} u_{ax} & 0 & 0 \\ 0 & u_{ay} & 0 \\ 0 & 0 & u_{az} \end{pmatrix} \cdot \begin{pmatrix} \lambda_x \\ \lambda_y \\ \lambda_z \end{pmatrix} = D(u_a)\vec{\lambda}. \quad \textbf{(4)}$$

It is important to account for the most general case where the scale factor (which again converts from voxel space to image space) is not known. This scenario typically occurs when A is recovered by registering the US image to some a priori known model including pre-acquired MRI or CT volume (or phantom) given in voxel space. In the linear formulation of the problem, we will use the linear operator *vec* and the *Kronecker product* ($\otimes$) [14]. Using the following property of the *Kronecker product*:

$$vec(CDE) = \left(C \otimes E^T\right) vec(D) \tag{3}$$

One can rewrite equation 1 as:

$$\left(R_a \otimes R_b\right) vec\left(R_x\right) = vec\left(R_x\right), \tag{4}$$

$$\left(I_3 \otimes t_b^t\right) vec\left(R_x\right) + \left(I_3 - R_a\right) t_x - D_u \lambda = 0 \tag{5}$$

From (4) and (5), we can transform the whole problem ($AX=XB$) into a single homogeneous linear system:

$$\begin{bmatrix} I_9 - R_a \otimes R_b & 0_{9*3} & 0_{9*3} \\ I_3 \otimes t_b^t & I_3 - R_a & -D_u \end{bmatrix} \begin{pmatrix} vec\left(R_x\right) \\ t_x \\ \lambda_{3*1} \end{pmatrix} = \begin{pmatrix} 0_{9*1} \\ 0_{3*1} \end{pmatrix} \tag{6}$$

The solution for this homogeneous linear system could be given by finding the *null space* Ψ, which is a subspace in R^{15}. Then the unique solution could be extracted from the null space using the unity constraint to the first 9 coefficients representing the R_x. In case of noise-free data, this method guarantees orthogonality but not normality of the recovered R_x, which can be easily fixed [15] as follows:

$$R_x = \frac{sign(\det(V))}{\left|\det(V)\right|^{1/3}} V$$

Where *sign* is a sign function that returns the sign of *det(V)*, $V=vec^{-1}(v)$ and v is any vector in the *null space* Ψ. In the case of noisy data, one can project the estimated R_x into *SO(3)* manifold, and get a corresponding least squares solution. Obviously, one motion is not enough to recover all the parameters. In fact, two independent motions [16-19] (three poses) with non-parallel axes is sufficient to recover a unique solution for $AX=XB$. However, another solution can be described in where the system is solved in two steps: first extract the rotation as in (7), and then solve for the translation and scale as in (8).

$$\begin{pmatrix} I_3 - R_{a1} \otimes R_{b1} \\ I_3 - R_{a2} \otimes R_{b2} \end{pmatrix} vec(R_x) = 0 \tag{7}$$

$$\begin{pmatrix} I_3 - R_{a1} & -D_{a1} \\ I_3 - R_{a2} & -D_{a2} \end{pmatrix} \begin{pmatrix} t_x \\ \lambda_{3*1} \end{pmatrix} = \begin{pmatrix} -R_x t_{b1} \\ -R_x t_{b2} \end{pmatrix} \tag{8}$$

We have extended this solution method to account for inhomogeneous scale in the three coordinate axes [8,20]. Prior to this work, we have exploited this closed form formulation to solve the calibration problem based on various mechanical phantoms including the double-wedge phantom [21], z-shape phantom [8], and thin-wall phantom [20]. In all these methods, phantoms were built in a way to assist estimation of *A's*, which is the relative motion between successive US frames as shown in Figure 2. Our present task reduces to recovering *A's* as we are scanning real tissue and collecting the corresponding *B's* from the tracker, and then obtaining the calibration by solving the homogenous linear system in equation (6). Obviously, recovering *A's* from real-time US sequences is a tracking problem instead of feature segmentation from static US phantom images. Tracking the 6 DOF of *A's* based on 3DUS data is considered a straight forward problem. The main challenge lies in the full recovery of the *A's* based on 2DUS data. The in-plane motion parameters can be recovered with sub-pixel accuracy in real-time, using speckle based tracking algorithms applied to the B-mode images. The out-of-plane motion parameters, however, appear to be difficult to recover from 2DUS data. In this paper, we recover *A's* through careful algebraic analysis of degenerate special motions utilizing the closed form formulation in (6). In general, a special or degenerate motion doesn't lead to unique optimal total, 6DOF, calibration. However these special motions (translation, planar or rotation about an axis) as shown in 2.1-2.3 can be used to partially calibrate the US system.

Translation Motion

This motion scenario is realized by moving the 2D/3D US probe in translational sweep (without rotation) to collect nearly parallel stack of images and/or series of 3D slabs. Also it can be shown in a panoramic scan where the images can be stitched together without introducing a relative rotation. Given this kind of motion, $R_b = R_a = I_3$, leading to, $R_x * t_{bi} = t_{ai}$ where i denotes the motion. Using the property of the *Kronecker product* in (3)

$$ {}_{3*9}\left(I_3 \otimes t_{bi}^T\right) *_{9*1} vec\,(Rx) = t_{ai}\,, \text{ we have} $$

$$ t_{ai} = \begin{bmatrix} \lambda_x * u_{ai}(x) \\ \lambda_y * u_{ai}(y) \\ \lambda_z * u_{ai}(z) \end{bmatrix} = \begin{bmatrix} u_{ai}(x) & 0 & 0 \\ 0 & u_{ai}(y) & 0 \\ 0 & 0 & u_{ai}(z) \end{bmatrix} \begin{bmatrix} \lambda_x \\ \lambda_y \\ \lambda_z \end{bmatrix} = D\left(u_{ai}\right)\vec{\lambda} $$

Three independent translations are sufficient to obtain a full-rank system. Solving for R_x and the three scale factors:

$$ {}_{9*9}\left[\overbrace{\begin{pmatrix} \left(I_3 \otimes t_{b1}^T\right) \\ \left(I_3 \otimes t_{b2}^T\right) \\ \left(I_3 \otimes t_{b3}^T\right) \end{pmatrix}}^{M}\right] *_{9*1} vec\,(Rx) = \begin{pmatrix} t_{a1} \\ t_{a2} \\ t_{a3} \end{pmatrix} = \begin{bmatrix} D\left(u_{a1}\right) \\ D\left(u_{a2}\right) \\ D\left(u_{a3}\right) \end{bmatrix} * \begin{pmatrix} \lambda_x \\ \lambda_y \\ \lambda_z \end{pmatrix} $$

$$ vec(Rx) = \underbrace{\frac{1}{\Delta}\left[I_3 \otimes \overbrace{(t_{b2} \times t_{b3})}^{v1} \quad I_3 \otimes \overbrace{(t_{b3} \times t_{b1})}^{v2} \quad I_3 \otimes \overbrace{(t_{b1} \times t_{b2})}^{v3} \right]}_{M^{-1}} * \begin{bmatrix} D(u_{a1}) \\ D(u_{a2}) \\ D(u_{a3}) \end{bmatrix} * \begin{pmatrix} \lambda_x \\ \lambda_y \\ \lambda_z \end{pmatrix} $$

Where $\Delta = det(t_{b1}, t_{b2}, t_{b3})$, Using Khatri-Rao product [14] which defined as:

$_{q\times u}F\circ_{t\times u}G=\left[F_1\otimes G_1 \quad F_2\otimes G_2 \quad \cdots \quad F_u\otimes G_u\right]$, and the following fact

$vec(\mathrm{AVD})=(\mathrm{D}^{\mathrm{T}}\circ \mathrm{A})vecd(\mathrm{V})$, where *vecd* is *vec* operator over diagonal elements.

$$vec(Rx)=\frac{1}{\Delta}\left[\overbrace{\begin{pmatrix}I_3 & I_3 & I_3\end{pmatrix}}^{D}\circ\overbrace{\begin{pmatrix}v_1 & v_1 & v_1 & v_2 & v_2 & v_2 & v_3 & v_3 & v_3\end{pmatrix}}^{A}\right]*\underbrace{\begin{bmatrix}D(u_{a1})\\ D(u_{a2})\\ D(u_{a3})\end{bmatrix}*\begin{pmatrix}\lambda_x\\ \lambda_y\\ \lambda_z\end{pmatrix}}_{V}$$

$$vec(Rx)=\frac{1}{\Delta}vec(A*V*D^T),\ \text{from linearity of vec operator}$$

$$Rx=\frac{1}{\Delta}A*V*D^T=\frac{1}{\Delta}\begin{bmatrix}\lambda_x(u_{a1}(x)v_1+u_{a2}(x)v_2+u_{a3}(x)v_3)\\ \lambda_y(u_{a1}(y)v_1+u_{a2}(y)v_2+u_{a3}(y)v_3)\\ \lambda_z(u_{a1}(z)v_1+u_{a2}(z)v_2+u_{a3}(z)v_3)\end{bmatrix}^T$$

We have obtained a closed-form solution that recovers an anisotropically scaled rotation matrix from three independent translations. We can recover the three scale factors by applying the unit constraint on each column vector, and recover the underlying rotation by then rescaling the columns to be unit vectors. This basically proves that three independent motions are sufficient to recover the rotation and the three scale factors. However, the third motion is not even necessary. It can be shown [15] that given two independent motions t_{b1}, t_{b2}, the third constraint comes from the cross-product between t_{b1}, t_{b2}.

In order to map this analysis to our application, several requirements must be considered. The ultrasound machine generates real-time 2D US pixel-map, meaning that we have only two unknown scale factors in x and y, denoted as λ_x and λ_y. With sweeping probe motion we obtain multiple poses which suggests folding the closed form representation into a least squares problem. Starting from the following equation:

$$\begin{aligned}&Rx*t_{bi}=t_{ai},\ \text{we have}\\ &t_{ai}=\begin{bmatrix}\lambda_x*u_{ai}(x)\\ \lambda_y*u_{ai}(y)\\ 0\end{bmatrix}=\begin{bmatrix}\lambda_x & 0 & 0\\ 0 & \lambda_y & 0\\ 0 & 0 & \lambda_z\end{bmatrix}\begin{bmatrix}u_{ai}(x)\\ u_{ai}(y)\\ 0\end{bmatrix}=D(\vec{\lambda})u_{ai}\\ &\begin{bmatrix}t_{b1} & t_{b2} & \cdots & t_{bn}\end{bmatrix}=Rx^TD(\vec{\lambda})\begin{bmatrix}u_{a1} & u_{a2} & \cdots & u_{an}\end{bmatrix}\end{aligned}\qquad (9)$$

The solution of this equation can be achieved in many ways. One can solve non-linearly for the three rotations and the two scale factors (λ_x, λ_y). Alternatively, one can solve linearly for the nine parameters of the scaled rotation and perform QR factorization with positive scale factor constraints. Or simply, apply the norm constraint on (9) as follows:

$$\left\|Rx*t_{bi}\right\|^2=\left\|t_{bi}\right\|^2=\left\|D(\vec{\lambda})u_{ai}\right\|^2={u_{ai}}^TD(\vec{\lambda})^2u_{ai}$$

This allows solving for both (λ_x, λ_y). After recalculating the scaled u_{ai}, we obtain two sets of points governed by an *SO(3)* rotation matrix that can be recovered with Horn's method [22].

Planar Motion

Planar motion is more general as it also allows, in addition to translation, in-plane rotation, referred to as 'Motion I' in Figure 4. This type of sweeping probe motion is commonly applied clinically. With this general motion, one can recover both rotation and anisotropic scale factors as shown before, but it will not yield a full recovery of the position offset t_x. By applying (6) we obtain:

$$\begin{bmatrix} I_9 - R_{ai} \otimes R_{bi} & 0_{9*3} \\ I_3 \otimes t_{bi}^t & -D_{ui} \\ \vdots & \end{bmatrix} \begin{pmatrix} vec(R_x) \\ \lambda_{3*1} \end{pmatrix} = \begin{pmatrix} 0_{9*1} \\ 0_{3*1} \\ \vdots \end{pmatrix}, \text{and} \tag{10}$$

$$\begin{bmatrix} (I_3 - R_{ai}) \\ \vdots \end{bmatrix} t_x = \begin{bmatrix} D_{ui}\vec{\lambda}_{3*1} - (I_3 \otimes t_{bi}^t) vec(R_x) \\ \vdots \end{bmatrix} \tag{11}$$

Note that when $Rb = Ra = I_3$, equation (10) becomes similar to the pure translation case in (9). Also note that equation (11) is always under constraint as $(I_3\text{-}R_a)$ has rank 2, regardless to the number of in-plane rotations, meaning there is no single solution for t_x and the general solution will have exactly one (the number of unknowns minus the rank) arbitrary scale factor ζ. So the solution can take the form:

$$t_x(\zeta) = t_\circ + \zeta * t_n$$

where ζ is the unknown scale factor and t_o is a unique solution in the plane of motion (2-dimensional), since $(I_3\text{-}R_a)$ has rank 2. t_n is the normal to the plane of motion (Figure 3). In our case, if the plane of motion is the US image plane (the x-y plane), t_n may equal $(0, 0, 1)^T$, which is a unit vector in the z-direction and thus perpendicular to the plane of motion.

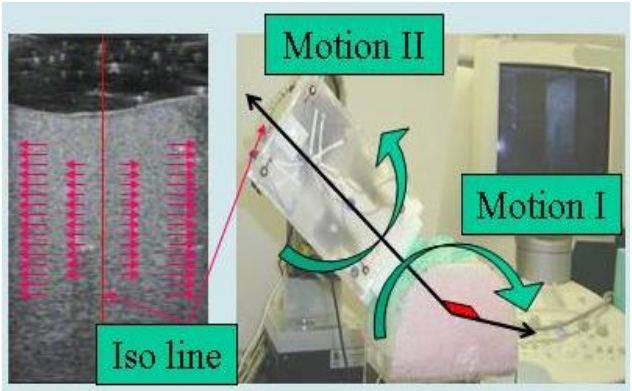

Figure 4: Experimental system and an illustration for the two suggested special motions. 'Motion I' indicates a planar motion, and 'Motion II' indicates a rotation about an axis.

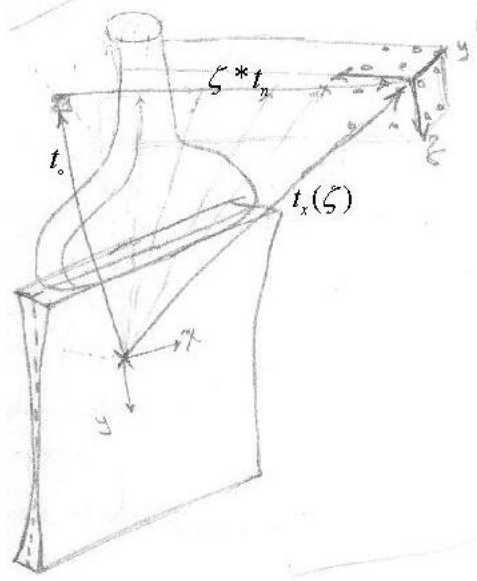

Figure 3: Illustration showing the unknown ζ.

Rotation about an axis

Assuming that we have R_x, λ_x, and λ_y, the next step is to recover either ζ in $t_x(\zeta)$, or t_x.. By substituting R_a from equation (1.b) into (1.c) we get the following equation:

$$R_x R_b R_x^T t_x + t_a = R_x t_b + t_x \tag{12}$$

In this equation we know everything except t_a, and t_x. For general "n" motions, equation (12) gives 3n constraints while leaving (3n+3) unknowns, 3n for t_{ai} and 3 for t_x, or (3n+1) unknowns, 3n for t_{ai} and 1 for ζ. There are basically two approaches to resolve this imbalance and solve for ζ or t_x. The first approach suggests estimating t_{ai} for all n motions. t_{ai} can be recovered by feature/speckle tracking in 6DOF, which is a straightforward task once we have continuous 3DUS data. However, in case of 2DUS data, the method is reliable to recover the in-plane 3DOF but it suffers from inevitable drift in recovering the out-of-plane 3DOF [23]. Currently, the authors are developing more reliable out-of-plane motion estimation algorithms. In this paper we adopted the second approach, which suggests utilizing a special motion, Figure 4, that would group all t_{ai} in a known relation instead of having to estimate all t_{ai}. Thus, one can easily recover t_x or ζ in $t_x(\zeta)$ as follows:

$$t_{a,k} = R_x t_{b,k} + (I - R_x R_{b,k} R_x^T) t_x,$$

The special relation/motion we are proposing here is the following:

$$t_{a,1} = t_{a,2} = \cdots t_{a,n}$$

$$R_x^T t_{a,k} = \frac{1}{n}\sum_{k=1}^{n} t_{b,k} + R_x^T t_x - \frac{1}{n}\sum_{k=1}^{n} R_{b,k} R_x^T t_x$$

This equation can be solved for either t_x as shown above or for ζ in case of having $t_x(\zeta)$.

3. MATERIALS AND METHODS

Experimental System

In our experimental prototype (Figure 4), we used a SONOLINE Antares US scanner (Siemens Medical Solutions USA, Inc. Ultrasound Division, Issaquah, WA), with a Siemens VF 10-5 linear array probe. The patient was replaced with a tissue mimicking agar phantom. The US probe was held against the phantom in a rigid acrylic holder mounted on an adjustable steady arm. The arm had a dual purpose: to adjust the spatial position of the tracked US probe over the calibration phantom, and to ensure temporal synchronization between the tracker and the US scanner. Multiple optical markers were attached to the probe holder, which then were tracked by an OPTOTRAK device (Northern Digital Inc.).

The tissue mimicking phantom provides realistic images of fully developed speckles. Its construction is based on a recipe by Fenster *et al.* [24]. Three percent by weight of agar gel (A-7002 Agar, Sigma-Aldrich, St. Louis, MO) was added to distilled water, with three percent by weight 50μm cellulose particles (S-5504 Sigmacell, Sigma-Aldrich), and with seven percent by volume glycerol (W25250, Sigma-Aldrich). The mixture was heated to 92 C°, stirred constantly, gradually cooled to 60 C°, and then poured into a container mold. We also introduced specular features and structures to mimic bone appearance and to allow for testing algorithmic performance under different echogenicity conditions.

Algorithm Workflow

The workflow in the real-time self-calibration QC procedure is described in Figure 5. The *Acquisition Module* receives the US video signal and tracker readings, from which it prepares synchronized indexed sequences of images and tracking information. The *Motion Analyzer* sorts out the types of motions in these sequences and sends a control signal for the *Real-time Tracker*, which recovers the *A* matrices. Finally, the *AX=XB* solver receives corresponding *A* and *B* data, and recovers the *X* calibration matrix. The *Quality Control* unit analyzes the new calibration and compares it with previous runs. In case of suspected discrepancy, an appropriate *Action* is initiated to deal with a hazard condition. The action could range from generating a warning message to demanding a halt of the procedure and full recalibration of the system.

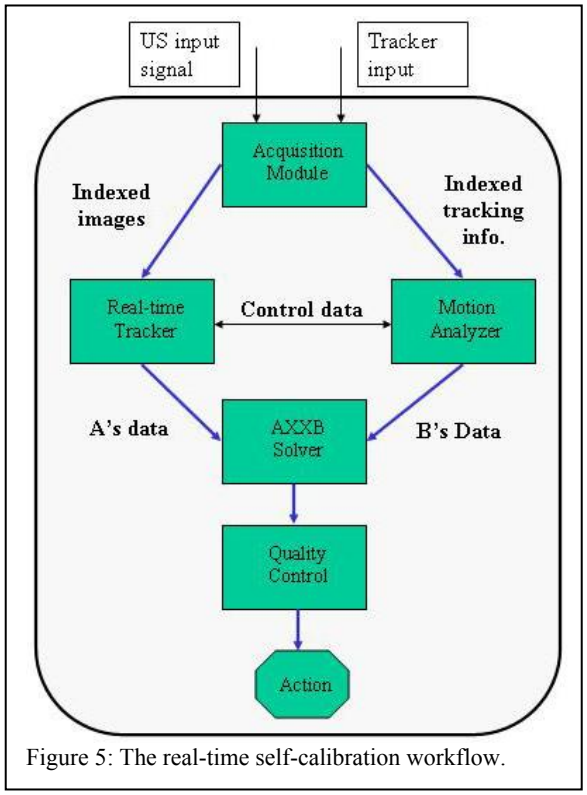

Figure 5: The real-time self-calibration workflow.

Real-time Tracker

As mentioned above, the role of Real-time Tracker is to recover the *A* matrices, the motion of the US image in construction frame, as it was described in Figure 2. What is necessary is to compute the relative motion in pairs of ultrasound images for which the absolute (tracked) motion is known. We accomplish this using direct image registration methods similar to those described in [25]. Specifically, we introduce an intermediate "warped" image representation *W* defined as:

$$W(u,t;p,\alpha) = I(Rot(\alpha) * u + p)$$

where $u=(x,y)^T$ is an image location, P is a translation offset, and α is an interframe rotation. Let $W(t; P, \alpha)$ denote the column vector constructed by stacking the value of W for all possible image locations u. We then compute an estimate of the offset (P_t, α_t) between images at time t and $t+d$ by iterating the following equation:

$$(p_t^k, \alpha_t^k) = (p_t^{k-1}, \alpha_t^{k-1}) + J^{\mp}(W(d+t; p_t^{k-1}, \alpha_t^{k-1}) - W(t;0,0))$$

where $J^{\mp}$ denotes the pseudo-inverse of the Jacobian matrix of W with respect to P and α. The values of (P_t, α_t) is taken from the previous frame.

4. EXPERIMENTS AND RESULTS

We used the experimental system to collect 5 datasets, altogether containing 20 motions in B-mode with a rectangular view and 8 cm depth. One of the datasets contained 4 motions and was obtained under a faulty condition: we purposely flipped lateral polarity of the B-mode image to simulate a common operator error. Table 1 shows the rotation and scale reported by the self-calibration QC system.

	Magnitude of rotation (Rodrigues form)	Scale in x and y (mm/pixel)	
Dataset-1	3.163	0.22	0.26
Dataset-2	3.072	0.23	0.26
Dataset-3	2.992	0.23	0.27
Dataset-4	3.008	0.23	0.29
Dataset-5	0.086	0.24	0.27

Table 1: QC system report on rotation and scale

In testing the image tracker, we used d=10 step size, for which images were matched with an RMS gray-scale error of less than 2% of signal value, suggesting a registration error of less than 1/10 pixel [25].

The heart of the self-calibration QC system, as seen in Figure 5, are the real-time image tracker and *AX=XB* solver. The image tracker is sensitive to the step *d* between registered images, while the *AX=XB* solver is sensitive to the number and type of motions used to recover the calibration parameters. The upper graph in Figure 6 illustrates the relation between the recovered scale and number of images and the step size *d* taken in the image registration algorithm. The "bad" case appears in the upper graph for the first 30 images and the "good" case is in the lower graph. Note that the number of images can be represented by the scanning time, where 1 second corresponds to 33 frames, sweeping over a certain distance covered with the given scanning velocity. The x-axis represents the number of frames used in the *AX=XB* solver and the y-axis is the scale ratio in mm/pixel. The upper figure is for λ_x, the lower is for λ_y. Figure 6 also shows convergence for the scale ratio under different image registration steps (small *d*: 1, 3, and 5; large *d*: 10, 20, 30, and 40). Note that as we increase the step size, we also introduce a delay equal to the step size before we start estimating a given parameter. This is because we must wait for the d^{th} image to arrive.

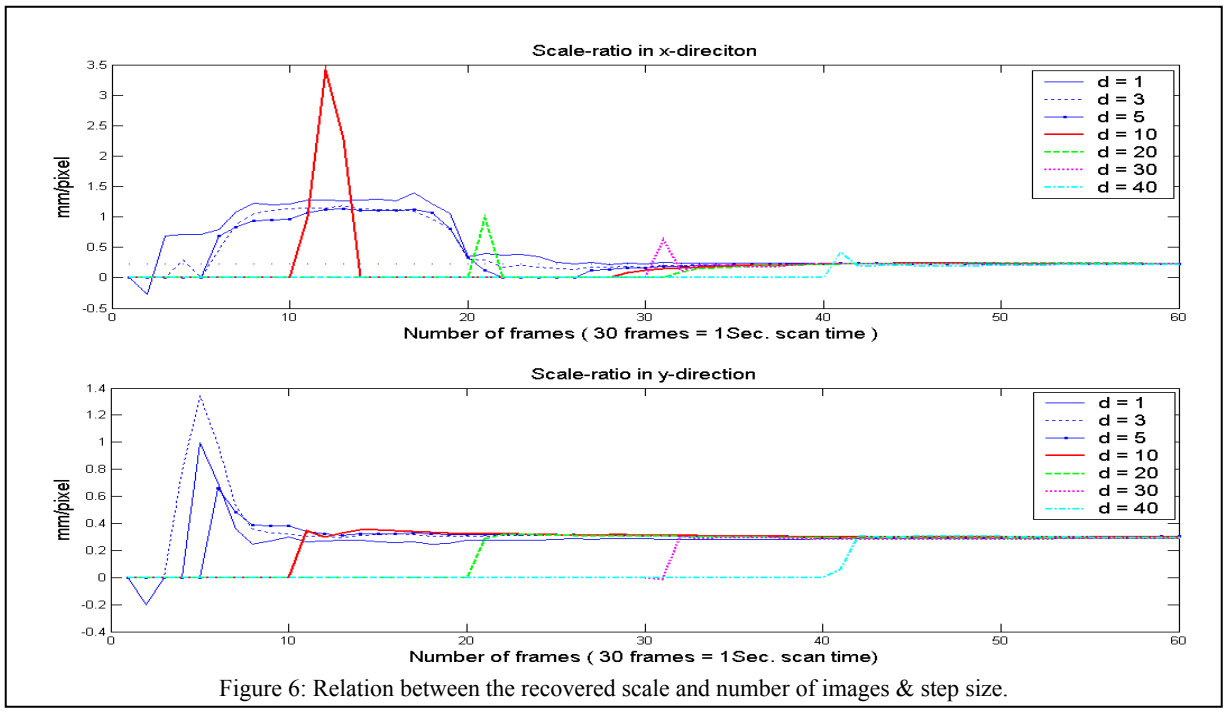

Figure 6: Relation between the recovered scale and number of images & step size.

We have found that steps larger than 40 frames are not reliable to track and predict the motions of the speckle patterns. At the same time, these kernels are temporarily distant, suggesting that we have to wait for about 2 seconds to detect a

faulty condition. However, small tracking steps do need a few readings to start convergence, due to the small motions they deliver to the *AX=XB* solver. Note that the convergence for *d= 1, 2, and 3* appears after 20 small motions for λ_y and appears after 30 small motions forλ_x, This is mainly due to the type of motion present. The intuition behind this is that we can't estimate a scaling parameter in a direction normal to the direction of motion. Similarly, favorable results were obtained for the rotation component, as shown in figure 7. We can conclude that given the right motion, a kernel of 10 steps (d=10) converges in 10-20 steps, meaning 0.3-0.6 seconds with a total travel of ~1.5mm (scanning speed @ 3mm/sec).

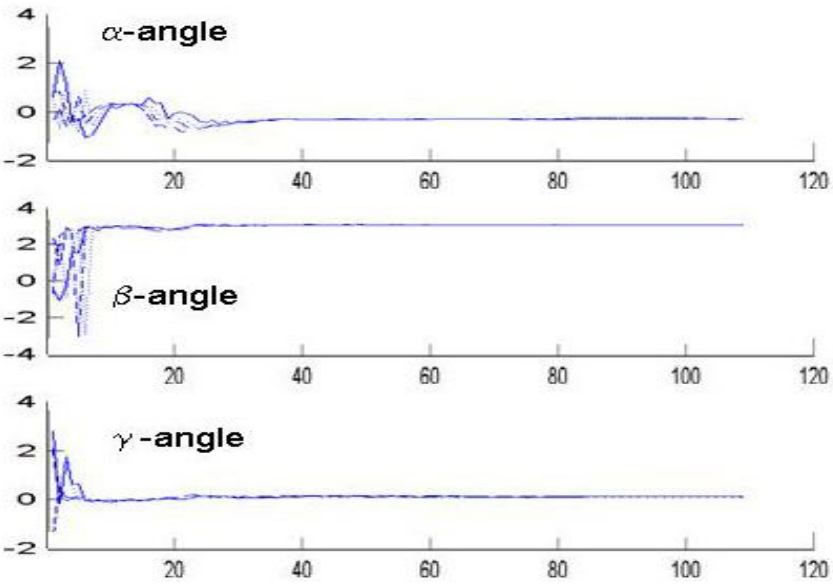

Figure 7: Similar convergence for the three rotation angles (α,β,γ) under 4 different small steps d=(1,2,4,5).

Conclusion and Future Work

In general, the self-calibration QC system reported the calibration matrix robustly and consistently. It recovered the correct calibration parameters under normal working conditions by monitoring the constancy of calibration matrix and did not produce false alarms. It also managed to distinguish the faulty condition by catching an outlier calibration matrix. By far the most significant work item in progress is extending the self-calibration QC framework to estimate the out-of-plane free motion of the US probe, thereby providing full calibration in-vivo, real-time, as the patient is being scanned, which will obviate phantom-based calibration. The real-time performance of the self-calibration QC system allows for averaging hundreds of independent calibrations from a single sweep, which in turn promises to retire cross-wire based reconstruction accuracy evaluation and at last make US calibration free from any phantom whatsoever. We will also compare the accuracy of our current self-calibration against published off-line calibration methods. Last but not least, the sensitivity and specificity of the self-calibration QC system will be examined. A clinical-grade QC system must catch all faulty conditions (high sensitivity), yet it must not halt the clinical intervention with producing false alarm (high specificity). Altogether, the combined QC and self-calibration system appears to have high practical utility for clinical departments that use and maintain tracked ultrasound systems. Finally, the authors acknowledge the financial support from the NSF #EEC 9731478 and Siemens Corporate Research.

REFERENCES

1. Thomas N., Dolores H. P., "Three-Dimensional Ultrasound Imaging", Ultrasound in Med. & Biol. Vol. 24, No. 9, pp. 1243-1270, 1998;

2. Boctor Emad M., Viswanathan A, Pieper S, Choti M, Taylor R, Kikinis R, Fichtinger G, "CISUS: An integrated 3D ultrasound system for IGT with modular tracking interface", IEEE SPIE Medical Imaging 2004, Proc. SPIE Int. Soc. Opt. Eng. 5367, pp. 247-256, May 2004.
3. Langen KM, Pouliot J, Anezinos C, et al. Evaluation of ultrasound-based prostate localization for image-guided radiotherapy. Int J Radiat Oncol Biol Phys. 57(3):635-44;
4. Carr J., Surface Reconstruction in 3D Medical Imaging, Ph.D. thesis, University of Canterbury, Christchurch, New Zealand, 1996;
5. Prager R. W., Rohling R. N., Gee A. H., and Berman L., "Rapid Calibration for 3-D Freehand Ultrasound," *US in Med. Biol.*, 24(6):855-869, 1998;
6. Pagoulatos N., Haynor D. R., and Kim Y., "A Fast Calibration Method for 3-D Tracking of Ultrasound Images Using a Spatial Localizer," *US in Med. Biol.*, 27(9):1219-1229, 2001;
7. Rousseau F., Hellier P., Barillot C., "A fully automatic calibration procedure for freehand 3D ultrasound," *In IEEE Int. Symp. on Biomedical Imaging, Washington D.C, Juillet 2002;*
8. Boctor E.M., Viswanathan A., Choti M.A., Taylor R.H., Fichtinger G., Hager G.D., "A Novel Closed Form Solution for Ultrasound Calibration," *In IEEE Int Symp. On Biomedical Imaging,* 2004;
9. Muratore DM, Galloway RL. Beam calibration without a phantom for creating a 3-D freehand ultrasound system. Ultrasound Med Biol. 2001 Nov;27(11):1557-66;
10. Detmer P. R., Bashein G., Hodges T., Beach K. W., Filer E.P., Burns D. H., and Strandness Jr. D. E., "3D Ultrasonic Image Feature Localization based on Magnetic Scanhead Tracking: In Vitro Calibration and Validation." *Ultrasound in Med. Biol.*, 23(4):597-609, 1996;
11. Boctor Emad M., Jain A., Choti M., Taylor R. H., Fichtinger G., "Rapid calibration method for registration and 3D tracking of ultrasound images using spatial localizer," *Proc. SPIE Vol. 5035,p. 521-532, Medical Imaging 2003;*
12. Blackall J. M., Rueckert D., Maurer Jr. C. R., Penney G. P., Hill D. L. G., and Hawkes D. J., "An image registration approach to automated calibration for freehand 3d ultrasound," *in Proc. of Medical Image Computing and Computer-Assisted Intervention, 2000;*
13. Mercier L., Langi T., Lindsesth F., and Collins D. L., A review of calibration techniques for freehand 3-D ultrasound systems. Ultrasound in Medicine & Biology, 31(4):449{471, 2005.
14. Brewer John W., "Kronecker Products and Matrix Calculus in System Theory", IEEE Trans. Circuits and systems, 25(9) Sep.1978;
15. Andreff N., Horaud R. and Espiau B., "Robot Hand-Eye Calibration Using Structure from Motion," *International J. of Robotics Research, 20(3), pp 228-248, 2001;*
16. Shiu Y. C. and Ahmad S., "Calibration of wrist-mounted robotic sensors by solving homogeneous transform equations of the form AX = XB", IEEE Trans. Robot. Automat., vol. 5, 16-29, (1989);
17. Tsai R. Y. and Lenz R. K., "A new technique for fully autonomous and efficient 3d robotics hand/eye calibration", IEEE Trans. Robot. Automat., vol. 5, 345-358, (1989);
18. Chen H., "A screw motion approach to uniqueness analysis of head-eye geometry". Proc. IEEE Int. Conf. on Computer Vision and Pattern Recognition, Maui, Hawaii, USA, 145-151,(June 1991);
19. Shi F.H., Wang J.H. and Liu Y.C., "An Approach to Improve Online Hand-Eye Calibration",In Proc. of IbPRIA 2005, LNCS 3522, 647-655, (2005);
20. Viswanathan A., Boctor Emad M., Taylor R.H., Hager G. D., Fichtinger G.: Immediate Ultrasound Calibration with Three Poses and Minimal Image Processing. MICCAI (2) 2004: 446-454;
21. Boctor EM, Iordachita I, Choti MA, Hager G, Fichtinger G., "Bootstrapped ultrasound calibration" Stud Health Technol Inform. 2005;119:61-6.
22. Horn BKP, "Closed-form solution of absolute orientation using unit quaternions" J Opt Soc Am A 1987;4:629–642.
23. Hassenpflug P., Prager R.W., Treece G.M. and Gee A.H., "Speckle classification for sensorless freehand 3D ultrasound. Speckle classification for sensorless freehand 3D ultrasound" Technical report CUED/F-INFENG/TR 513, Cambridge University Department of Engineering, March 2005.
24. Rickey DW, Picot PA, Christopher DC, and Fenster A, "A Wall-less Vessel Phantom for Doppler Ultrasound Studies," US in Med. Biol., 21, 1163-1175, 1995.
25. Hager G. and Belhumeur P., "Efficient region tracking with parametric models of geometry and illumination". IEEE Transactions of Pattern Analysis and Machine Intelligence, 20(10):1125–1139, 1998.